Research Article

Silicon Microchannel-Driven Raman Scattering Enhancement to Improve Gold Nanorod Functions as a SERS Substrate toward Single-Molecule Detection

Jaciara Bär, Anerise de Barros, Davi H. S. de Camargo, Mariane P. Pereira, Leandro Merces, Flavio Makoto Shimizu, Fernando A. Sigoli, Carlos César Bof Bufon, and Italo Odone Mazali*

Read Online

ACCESS | Metrics & More | Article Recommendations | SI Supporting Information
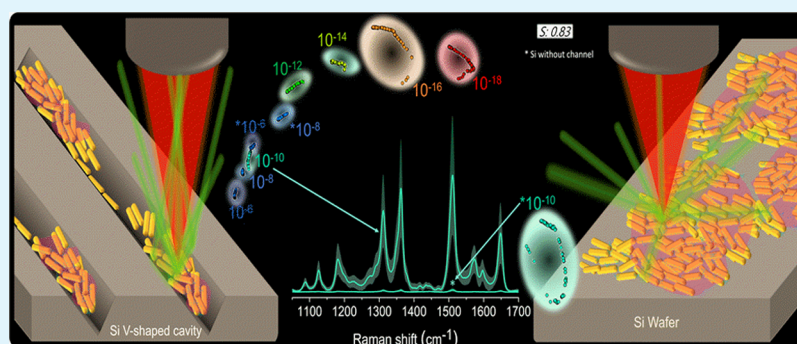
ABSTRACT: The investigation of enhanced Raman signal effects and the preparation of high-quality, reliable surface-enhanced Raman scattering (SERS) substrates is still a hot topic in the SERS field. Herein, we report an effect based on the shape-induced enhanced Raman scattering (SIERS) to improve the action of gold nanorods (AuNRs) as a SERS substrate. Scattered electric field simulations reveal that bare V-shaped Si substrates exhibit spatially distributed interference patterns from the incident radiation used in the Raman experiment, resulting in constructive interference for an enhanced Raman signal. Experimental data show a 4.29 increase in Raman signal intensity for bare V-shaped Si microchannels when compared with flat Si substrates. The combination of V-shaped microchannels and uniform aggregates of AuNRs is the key feature to achieve detections in ultra-low concentrations, enabling reproducible SERS substrates having high performance and sensitivity. Besides SIERS effects, the geometric design of V-shaped microchannels also enables a "trap" to the molecule confinement and builds up an excellent electromagnetic field distribution by AuNR aggregates. The statistical projection of SERS spectra combined with the SIERS effect displayed a silhouette coefficient of 0.83, indicating attomolar (10^{-18} mol L^{-1}) detection with the V-shaped Si microchannel.

KEYWORDS: SERS, SIERS, microchannel, three-dimensional hot spot, gold nanorods, single-molecule detection

1. INTRODUCTION

Surface-enhanced Raman scattering (SERS) is a crucial analytical tool for molecule fingerprints in ultrasensitive detection.[1−9] SERS effects are reported from the 1970s,[10−12] and since then, they have aroused a great awakening in the spectroscopy field as an analytical tool. The enhancement effect is provided by the electromagnetic (EM) interaction of light with metals, producing significant amplification of the laser field through excitation of plasmon resonances.[13] The excitation of plasmon resonances in a certain condition can be generated in metallic films of nanometer thickness, called surface plasmon resonance (SPR), and in metallic nanoparticles, called localized SPR (LSPR).[13] In the latter, the coupling of metallic nanoparticles as dimers, trimers, or large aggregates leads to a strong EM field enabling enhancement factors of 10^{10} to 10^{14} orders. The SERS signal is highly

dependent on the interparticle gap distance to maximize the EM field experienced by a molecule.[14,15] However, it is a long-standing challenge to control these couplings of nanoparticles at precise locations due to their small spatial volumes. Consequently, obtaining a SERS substrate with high response reproducibility in low-level sample concentrations is still an enormous challenge. Several strategies have been developed for a better performance of SERS substrates,[16,17] such as the aggregation of nanoparticles induced by organic solvents like

alcohols,[18] or using cucurbit[urils][19] molecules to form a large number of hot spots. Alternative SERS strategies have been reported for the analyte drying dynamics on a SERS substrate[20,21] and in situ analysis performed by microfluidic-type continuous flow methodologies.[22] de Barros et al.[20] used a SERS approach based on different dielectric environment analyses to explain the dependence of SERS signals in a relationship to the dynamic behavior of rhodamine 6G (R6G) when adsorbed on a gold nanorod (AuNR) surface.

Recently, some strategies have also been adopted for cavity SERS substrates covered with a metallic thin film (Ag or Au), in which the SERS effect is based on the SPR mechanism for noble metal substrates.[23−27] Surface cavity effects induced by the incident radiation are denominated "hot spot area".[28] The most significant advantage of a SERS substrate with a cavity is the hot spot region generated by the own cavity, increasing the probability of finding a high concentration of molecules under confinement.[28] For instance, Li et al.[28] fabricated a plasmonic SERS substrate in V- and W-shaped cavity arrays from anisotropic wet etching (AWE), with potassium hydroxide on a (100) silicon (Si) wafer. V- and W-shaped SERS substrates were evaluated using 4-mercaptopyridine as a probe molecule. The results reveal that the plasmonic W-shaped cavity array provides a signal intensity 3.34 times stronger than the plasmonic V-shaped cavity and analytical enhancement factor (AEF) of 2.99×10^5 and 9.97×10^5 for V- and W-shaped substrates, respectively. Finite difference time domain simulation data indicate an excellent performance of the SERS cavity substrate by the strong EM field generated between the cavity edges. The effect of EM field concentration on the cavity edge was also studied by Gu et al.,[24] routinely known as the waveguide concentrated EM field. A single Ag nanoparticle located in the waveguide concentrated EM field generates a 1000-fold increase in the local field, providing a SERS substrate comparable to those having aggregates of nanoparticles. Hybrid SERS substrates with a microchannel covered with a metallic gold film (Au-film) and AuNRs deposited along the microchannel length are used as a structured support to form a top dielectric grating spacer and Au mirror. The SERS performance is achieved by the leaking energy of the guided mode coupled or re-coupled to the LSPRs by reflection on the Au mirror.[29] In this way, Maimaiti et al.[30] demonstrated that a hybrid particle-on-mirror system could be used for extreme light confinement. The near field of a hybrid high-index dielectric particle on an ultra-flat Au mirror is highly enhanced in a gap region between silicon nanodisks and the Au-film surface. The system used for SERS and fluorescence enhancement shows efficiency comparable to those obtained using a purely metallic particle-on-mirror.

Light confinement effects were also demonstrated in Si cavities without metallic film coverage, where Si cavities under the wavelength excitation close to the width cavity act as a matrix increasing the Raman scattering efficiency for different substances embedded inside the cavities.[31−33] However, the structures of cavities without metallic films are still poorly explored in the literature, and the combination of substrates having Si cavities with metallic nanoparticles can be an excellent alternative to create efficient SERS substrates presenting high reproducibility. Based on that, we fabricate V-shaped microchannels on Si wafer substrates and demonstrate how the substrate geometry influences the Raman signal intensity without SPR or LSPR effects. V-shaped microchannels combined with side-by-side patterns of AuNR

aggregates is the key feature to promote SERS substrates, presenting high performance, sensitivity, and reproducibility. The V-shaped geometric design of the microchannel also acts as a "trap" to confine target molecules and build an excellent EM field distribution by AuNR aggregates. The excellent amplification of Raman scattering observed in V-shaped Si substrates without AuNRs was predicted from scattered field simulation and corroborated with experimental data, besides being compared to flat Si substrates. Raman and SERS measurements were obtained using (R6G) dye as a probe molecule, and the statistical projection of SERS spectra was employed to evaluate the sensitivity for both structures.

2. EXPERIMENTAL SECTION

2.1. Materials. V-shaped microchannels were fabricated in (100) Si/SiO$_2$ (2 μm thick) with a 9 × 9 mm size. 1,1,1,3,3,3-hexamethyldisilazane (HMDS), AZ nLOF 2020 photoresist, and AZ 726 MIF developer were purchased from MicroChemicals. Tetrachloroauric(III) acid trihydrate (HAuCl$_4$·3H$_2$O), hexadecyltrimethylammonium bromide (CTAB, ≥99%), and potassium hydroxide (KOH, 90%) were purchased from Sigma-Aldrich. Sodium hydroxide (NaOH, P.A.), hydrogen peroxide (H$_2$O$_2$, 30%), acetone (C$_3$H$_6$O, P.A.), acetone (C$_3$H$_6$O, VLSI, very large scale integration), and isopropyl alcohol (C$_3$H$_7$OH, VLSI) were purchased from Synth. R6G (99%) was purchased from Acros Organic. R6G aqueous solution was prepared at 10^{-3} mol L^{-1} stock solution in ultrapure water and diluted until 10^{-18} mol L^{-1}.

2.2. Instrumentation. A WS-650-23B spin coater from Laurell Technologies Corporation was used in the photoresist deposition. Direct-write photolithography machine MicroWriter ML3 was employed in the ultraviolet (UV) exposition. PlasmaProNGP80, (Oxford Instruments Plasma Technology) was employed in the reactive ion etching (RIE). Micrograph characterizations were performed with a 3D laser scanning confocal microscope—VK-X200 (Keyence), Wavelength—408 nm, violet, scanning electron microscopy (SEM), model FEI Quanta 250 FEG, and transmission electron microscopy, Zeiss Libra 120. Raman and SERS spectra were collected using a HORIBA Jobin Yvon T64000 Raman spectrometer coupled with an Olympus BX41 microscope and a charge-coupled device detector using incident radiation excitation of 633 nm from a He−Ne laser (Research Electro-Optics). The Raman analyses were evaluated using a 50× objective lens and one accumulation of 20 s exposition radiation. The crystalline silicon band at 520.7 cm^{-1} was used in spectrometer calibration.

2.3. Si(100) Microchannel Fabrication. V-shaped microchannels were fabricated in Si(100) substrates (9 × 9 mm) by AWE using 40% of KOH solution at 80 °C and a patterned SiO$_2$ mask to protect the demarcated Si regions from AWE. Previously to the AWE process, photolithography and RIE processes were used to pattern the SiO$_2$ mask. Figure S1 in the Supporting Information corresponds to the schematic illustration for each step used for the channel microfabrication. The Si(100) substrate was previously cleaned through immersion in acetone P.A., followed by immersion into the acetone and isopropyl alcohol VLSI grade for 40 min each and submitted to the oxygen plasma to remove the organic residuals. Subsequently, HMDS was applied on the Si surface using a spin coater (3000 rpm by 30 s) to improve the photoresist adherence and then, the substrates were heated to 100 °C for 3 min. The AZ nLOF 2020 negative photoresist was spread on the Si surface using the following spin-coating sequential steps: (i) 2000 rpm for 5 s; (ii) 3000 rpm during 30 s; and (iii) 1000 rpm for 5 s. The spin-coating process was optimized to ensure a uniform photoresist deposition on the Si surface, including the border of the sample. The photoresist films were soft-baked at 100 °C for 2 min. The pattern prepared consisted of 26 microchannels having a length of 5 mm and 4 μm width. The channels are 100 μm spaced for a set close to the sample edge and 20 μm for the central channels. Figure S2 illustrates the virtual mask, and

Scheme 1. Schematic Illustration of (a) AuNR Colloidal Suspension Deposition by Drop-Casting Methodology and (b) R6G Solution Adsorbed on AuNR Nanostructures in the V-Shaped Si Microchannel Substrate
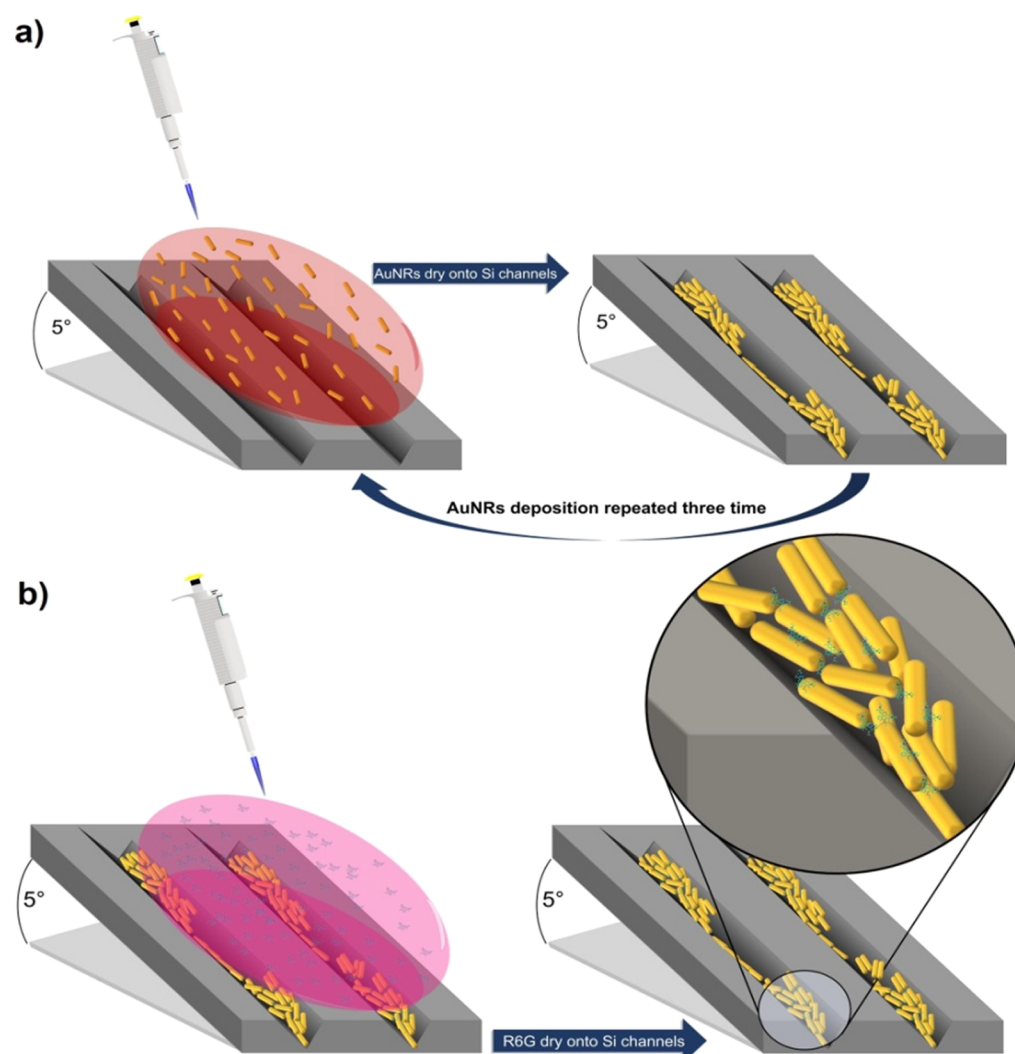
more details of exposition parameters are shown in Table S1 (Supporting Information).

2.4. SERS Substrate Fabrication. AuNRs were deposited on the V-shaped microchannel Si substrates through the drop-cast method, with deposition protocol adapted according to the procedure described by Ashkar et al.[34] First, the substrate was positioned with an inclination of 5° to favor the flow of the AuNR suspension by capillarity inside the V-shaped microchannels.[34] Sequentially, 100 μL of the AuNR colloidal suspension (stock) was diluted in 900 μL of ultrapure water and an aliquot of 10 μL of this AuNR suspension was dropped on the V-shaped Si microchannel substrates, followed by the addition of 3 μL of isopropyl alcohol. Then, the substrate was rotated 180° to promote the AuNR deposition across the length of the microchannels, keeping the same 5° tilt angle, and the AuNR drop is entirely dried after 2 h at room temperature. This process was repeated twice more, following the addition of AuNRs with isopropyl alcohol and the substrate position was altered by 180°. The same protocol deposition was performed to the flat Si substrate and R6G solution. Scheme 1a,b shows the representative steps of the sample preparation for Raman analysis. It should be noted that the synthesis of AuNRs was described in the Supporting Information and their respective characterizations (Figure S3 and S4).

2.5. Scattered Electric Field Simulation. Finite-element simulations were performed in COMSOL Multiphysics software. A 2-dimensional space coupled to the RF module (in-plane transverse electric waves) was employed to calculate the electric field scattered by the samples. The calculations were made along a representative sample cross section composed of free space (vacuum) and a Si substrate with a flat region and a V-shaped microchannel (Figure S5). At the sample surface/vacuum cross section, the flat Si counterpart was 115 μm long, whereas the V-shaped region was 65 μm long (Figure S5a). The V-shaped Si microchannel's physical dimensions are defined similarly to the patterned structure, that is, a 4.5 μm wide and 6.0 μm deep cavity (Figure S5e). The Si sample thickness is set as 50 μm without generality loss. A limited space ($240 \times 240 \ \mu m^2$ cross section) is defined surrounding the sample geometry, whereas the plane-wave scattering boundary condition is applied. As subdomain settings, the relative permittivity and permeability of each material (vacuum and Si) are given by the software library. The simulation is completed with the incoming electric field selected according to the laser wavelength used for the Raman spectroscopy analyses, that is, 633 nm. The plane wave propagates in the x-direction with an electric field polarization along the z-axis. For the mesh configuration (Figure S5b−e), triangular elements are used, with a custom mesh size employing 0.3 maximum element size scaling factor, 1.01 element growth rate, 0.5 curvature factor, and 0.1 curvature cutoff. Such parameters resulted in 43,145 subdomain elements for the finite-element calculation. The scattered electric field was calculated using the direct (UMFPACK) linear system solver. The absolute z-component of the scattered electric field was considered for the elucidation of the V-shaped microchannel influence on the Raman scattering compared to flat Si samples.
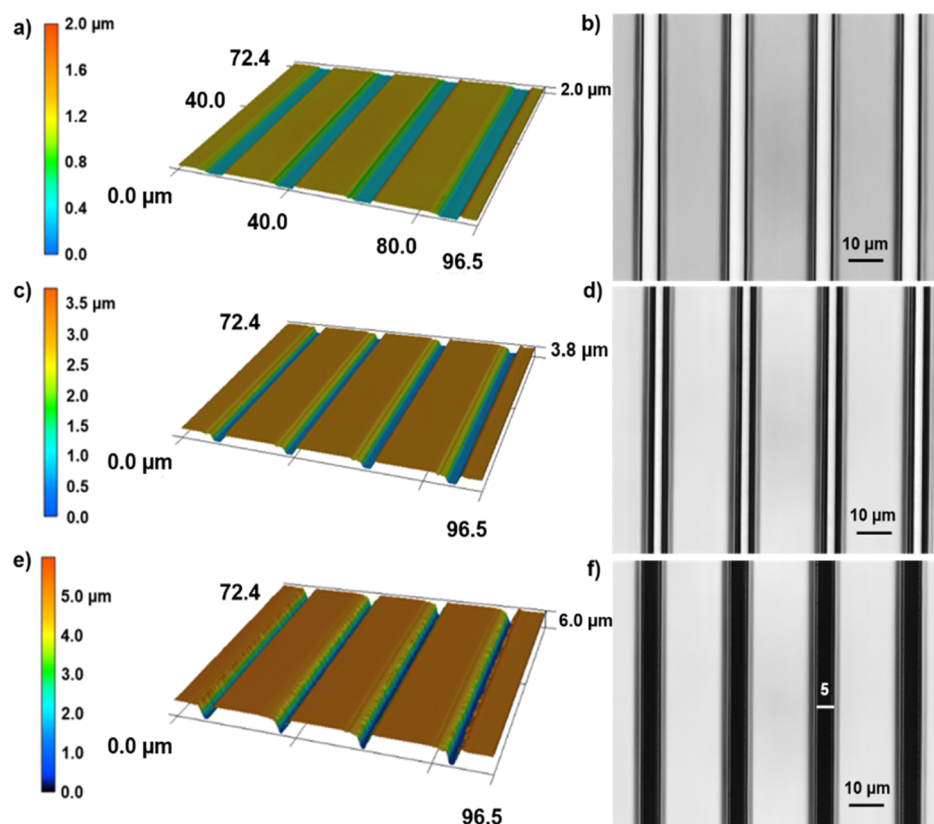
Figure 1. Three-dimensional and bidimensional confocal images were acquired during the AWE process monitoring. (a,b) Before the AWE process; (c,d) After 2 min of the AWE process. (e,f) After 4 min of the AWE process.

2.6. Statistical Analysis.

The visualization of Raman spectra is facilitated by multidimensional data projection techniques, such as classical scaling (CS),[35] interactive document mapping (IDMAP),[36] Sammon's mapping (SM),[37] and least square projection (LSP),[38] which comprise suite tools of the software PEx-Sensors.[39] Here, the whole spectra (1100 to 1700 cm^{-1}) are employed in the analysis, with no need of search or selection of Raman bands. They are dimensionally reduced from 446 to 2 dimensions with the FastMap algorithm, and the dissimilarities between samples are calculated using the Jaccard index. Since scattering effects are commonly observed in spectroscopic experiments, we applied the extended multiplicative scatters correction (EMSC) using MATLAB software to decrease the dispersion and improve the multidimensional data discrimination.

3. RESULTS AND DISCUSSION

The process of V-shaped Si microchannel fabrication has been carefully optimized to obtain a good uniformity and low groove along to the length of the microchannels and their walls. Figure 1a–f exhibits the patterned surface images acquired during the AWE process. Figure 1a,b corresponds to the substrate after the RIE process before starting the AWE process. In this step, the channel displays a depth of 2 μm, indicating that the SiO$_2$ mask in the patterned regions was entirely etched during the RIE process. Figure 1c,d corresponds to the substrate surface under the AWE process that lasted 2 min. Figure 1e,f corresponds to the substrate after 4 min of etching.

The previous confocal images show that the V-shaped microchannels are ready after 4 min of the AWE process. The top of the microchannel aperture in Si was etched during the process and designed to be ∼4 μm. The time required to get the V-shaped Si microchannels is directly related to the exposed surface area. Therefore, the microchannel aperture was designed for a faster etching process, leading to lower KOH consumption. Figure 1a,c,e reveals that the optimized microfabrication process promotes microchannels with a 6.0 μm depth and 5.0 μm aperture. The precise microchannel apertures were ∼4.5 μm, corroborated with SEM analyses (Figure 1c). Therefore, SEM micrographs are essential to verify the channel quality fabricated by the time parameters determined and observed through confocal images. In Figure 2a–d, it is possible to see the high quality of V-shaped Si microchannels, displaying an excellent uniformity and low grooved walls (see Figure S6; the V-shaped Si microchannels before the optimization process).

Flat, V-shaped Si bare substrates are evaluated by Raman analysis using R6G dye as a probe molecule. Figure 3a shows the average Raman spectra for R6G 10^{-3} mol L^{-1} obtained from the hundred set Raman spectra, illustrated in Figure 3b,c. We observed that the Raman signal in the presence of R6G is enhanced by 4.29 times by using the V-shaped Si microchannel bare substrate compared to the flat Si substrate. This increase in the Raman intensity is closely related to the geometric pattern designed on the Si substrate, and to better comprehend the effects involved, we performed finite-element calculations on the electric field scattered. Figure 4a shows the sample cross section considered in the electric field simulation, that is, flat and V-shaped Si substrates. For this, we considered an incoming plane wave (wavelength of 633 nm), in which the intensity of the scattered electric field (absolute z component) is normalized by the incoming electric field intensity (color scale), as shown in Figure 4b,c.
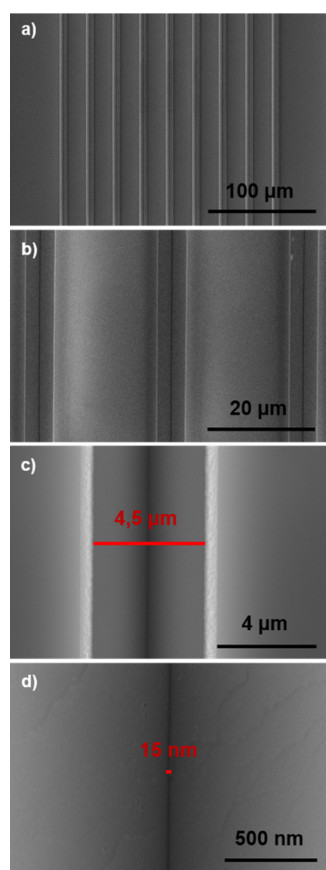
Figure 2. (a–d) SEM micrographs for V-shaped Si microchannel substrates in different magnifications.

In Figure 4b,c, the locations with maximum enhancement of scattered electric field can be noticed on the V-shaped microchannel edges and its vicinity, providing more interference patterns from the scattered electric field propagation. As a result, a Raman signal enhancement will occur in constructive interference regions, corroborating the result seen in Figure 3a. To better comprehend how these interference patterns can vary depending on the V-shaped substrate region, Figure 4d exhibits the absolute scattered electric field profiles obtained along lines 1−7, initially traced in Figure 4a. The profile lines show that the scattered field interference permeates all the space surrounding the V-shaped microchannel, including its substrate. The effective influence of the Si cavity on the scattered field can be quantitatively evaluated along with the intensification showed by profiles 2−6 in Figure 4d. Our calculation shows that, on average, the electric field intensification can reach up to 50 times the intensity of the incident radiation on the walls and edges of V-shaped microchannels. However, the electric field intensification should occur close to the sample surface to be a high-intensity region for the Raman signal.[40] On this subject, the V-shaped microchannel can intensify the scattered electric field in both the cavity and its vicinity, as demonstrated by the bright spots in Figure 4c and the profile line 4 in Figure 4d, respectively. In order to prove that the constructive interference patterns are explicitly generated by the V-shaped geometric design and occur as much in the cavity as in the microchannel vicinity, we monitored the characteristic Si band at 521 cm^{-1} in different V-shaped Si substrate regions, as illustrated in Figure S7.

The electric field intensification predicted by our theoretical calculation is confirmed by the Raman spectra acquired from both bare Si substrate structures (flat and V-shaped Si substrates). Figure 4e shows the average Raman spectra of the characteristic Si band at 521 cm^{-1}, whereas schematic representations for the calculated scattering behavior are shown in the insets (e.1) and (e.2). We observed an intensity increase of 1.82 times for the Si V-shaped microchannels when compared to the flat Si substrate. The measured Raman signal enhancement is attributed to the V-shaped microchannels on the Si surface, providing a distribution of Raman scattering high-intensity region supported by the calculated electric field intensification. We propose that the observed phenomenon herein called shape-induced enhanced Raman scattering
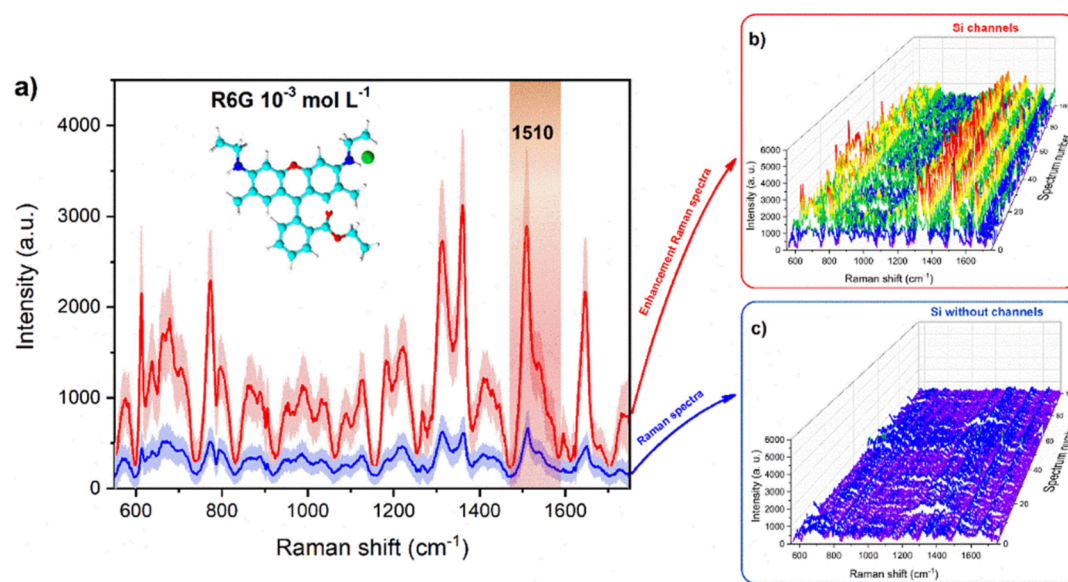
Figure 3. (a) Average Raman spectra for R6G 10^{-3} mol L^{-1} for bare V-shaped Si microchannel (red spectrum) compared to the bare flat Si (blue spectrum). (b,c) 100 Raman spectra of R6G acquired for the flat and V-shaped Si bare substrates. All analyses were taken using a 633 nm laser, with an 1 s exposition time and 1 accumulation (acc).
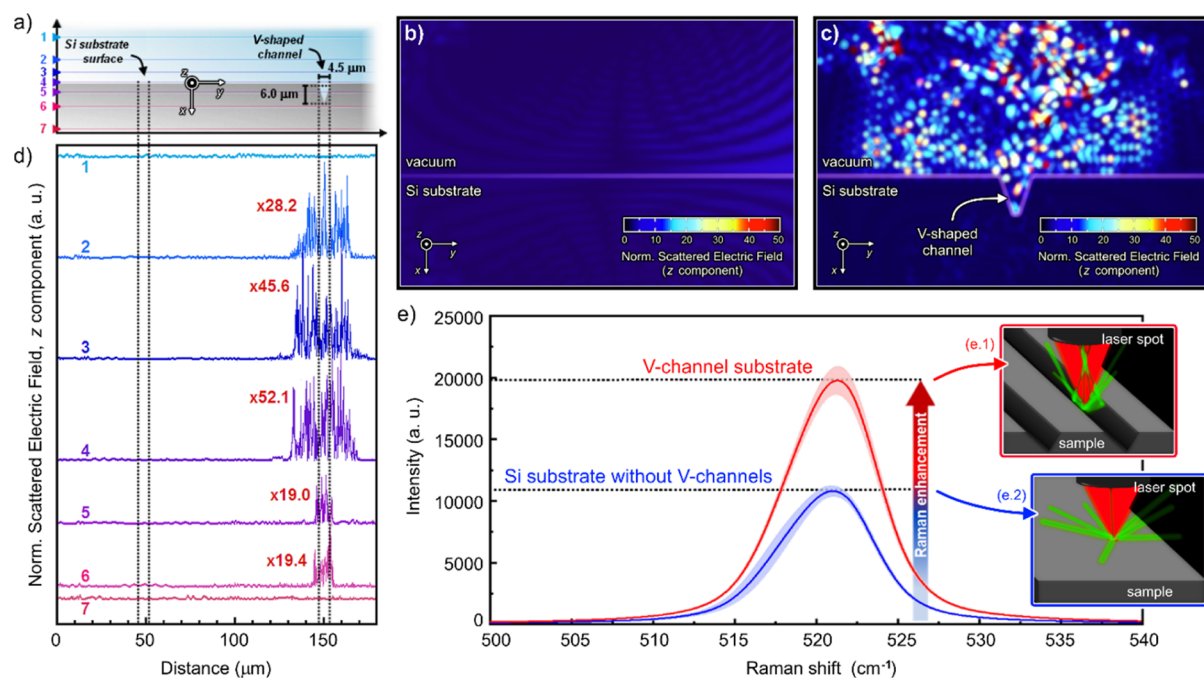
Figure 4. Finite-element simulation on substrates scattered electric field and bare Si substrate Raman scattering intensity; (a) cross-sectional sketch of the sample structure used in the simulation. Electric field (normalized by the incoming electric field intensity) scattered by the (b) flat Si substrate and the (c) V-shaped Si microchannel. (d) Normalized scattered electric field (z component) along the profile lines 1−7 of the (a). (e) Average Raman spectra for the flat and V-shaped Si substrates monitored by the Si band at 521 cm^{-1}. Schematic representations of the Raman scattering behavior predicted by the simulations are shown as insets (e.1,e.2). The Raman analyses were done in different substrate regions using a 633 nm wavelength laser with a 10 s exposition time and 1 acc.
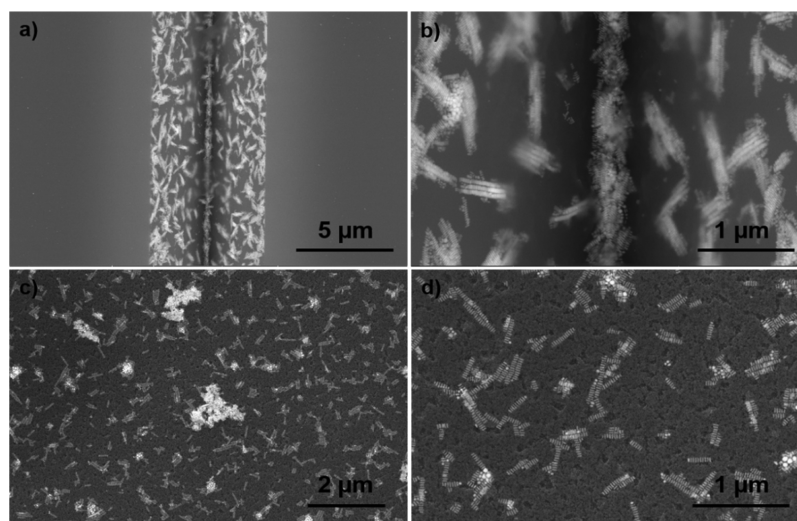
Figure 5. SEM images of AuNRs deposited in different Si substrates; (a,b) V-shaped Si microchannels substrate and (c,d) flat Si substrate.

(SIERS) is based on the electric field intensification caused by constructive interference patterns of light irradiated from the V-shaped cavity. The effect induced by the geometric design of microchannels on the Si substrate was also demonstrated by Mamichev et al.[33] Briefly, 1.0 μm cavities under the wavelength excitation close to the Si cavity width act as a matrix, increasing the Raman scattering efficiency for different substances embedded inside the cavities. The authors suggested that a partial light localization is formed within the cavities due to waveguide propagation of the excitation light. As a result, the effective volume of the medium interacts with the laser radiation, thus increasing the Raman scattering efficiency.

Consequently, the SIERS effect reported here is a valuable tool to improve the effect of metallic nanoparticles in SERS substrates, providing reproducible SERS substrates having high sensitivity to achieve single-molecule detection. In this way, the AuNR colloidal suspension is deposited on the flat and V-shaped Si substrates and characterized from SEM micrographs, as seen in Figure 5a−d.

The AuNR deposition is attended with an aliquot of isopropyl alcohol to decrease surface tension due to the high hydrophobicity of the V-shaped Si substrates. It improves the deposition of AuNRs inside microchannels, as shown in Figure 5a,b, avoiding the deposition between the microchannel
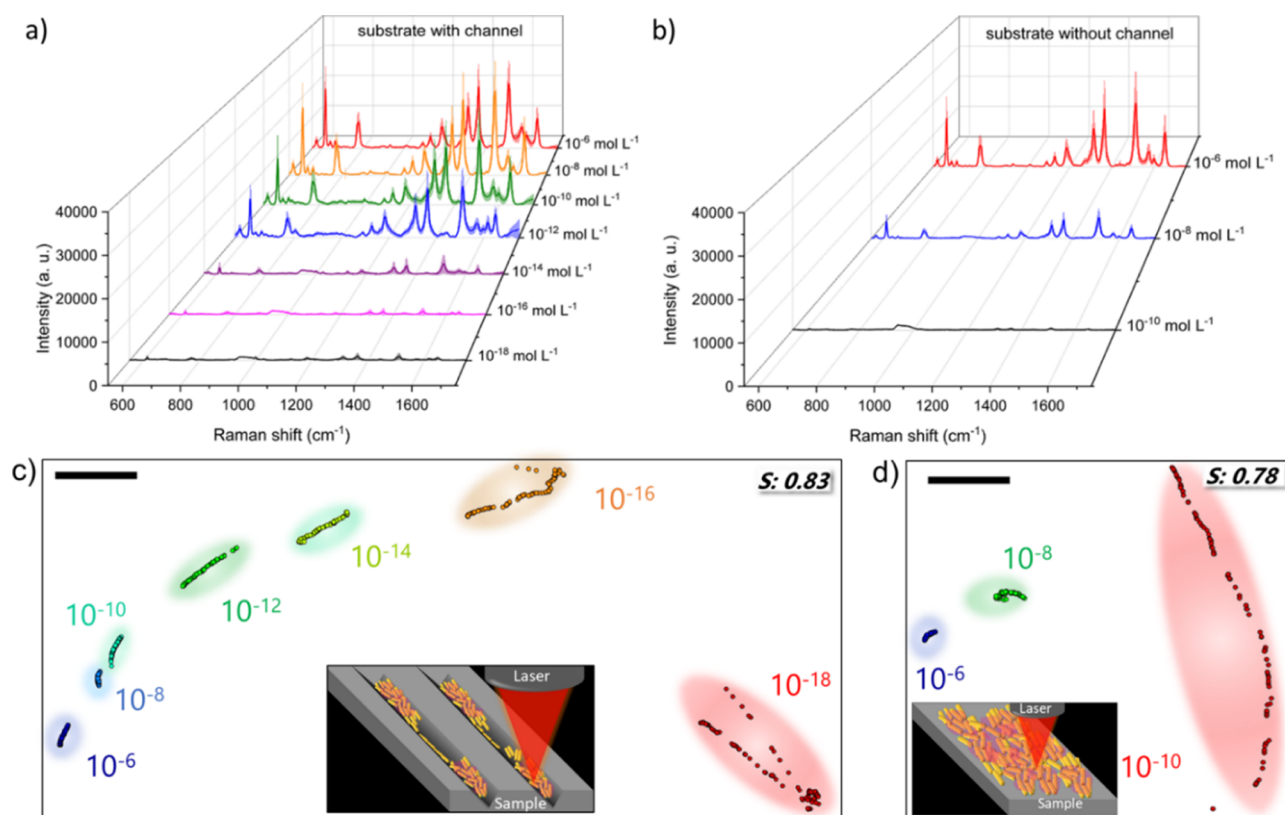
Figure 6. Average SERS spectra in different R6G concentrations for the V-shaped Si substrate with AuNRs (a) and flat Si substrate with AuNRs (b). The shading matches line corresponds to the standard error obtained for the set of 100 spectra collected. CS plots of corrected R6G Raman spectra (1100−1700 cm^{-1}) in different concentrations for (c) V-shaped Si substrate and (d) flat Si substrates modified with AuNRs. The black bar is only a guide to measure distances between data points. All analyses were taken in different substrates, using a 633 nm laser with exposition time of 20 s and 1 acc.

spacing on the top of the Si substrate. Interestingly, the AuNRs displayed an aggregate distribution pattern that is also observed for flat Si substrates in Figure 5c,d. Note that the AuNR aggregation occurs preferentially side-by-side, in the horizontal and vertical position arrangement. The side-by-side AuNR aggregation occurs due to the removal of the CTAB stabilizer surrounding AuNRs, induced by the addition of isopropyl alcohol.[18] Additional SEM micrographs (Figures S8 and S9) exhibit the coupling arrangement in different regions of flat and V-shaped Si substrates, respectively. Figure S10 shows an excellent AuNR distribution by sequential SEM images obtained along the V-shaped microchannel. The AuNR aggregation arrangements favor constructive interferences from the corresponding electronic oscillations, resulting in a more intensified field region relative to a single particle. Consequently, it creates a tremendous impact on the optoelectronic properties with the most desirable configuration for SERS applications.[21] Herein, the LSPR band of the colloidal AuNR solution is characterized at 715 nm, with the side-by-side AuNR arrangement favoring a blue shift in the LSPR band using a 633 nm excitation wavelength, which was already reported by our group.[20] Therefore, we are working on the resonance particle condition that leads to a significant intensified field. We evaluated the influence of SIERS effects in SERS substrates modified with AuNR nanostructures by collecting hundreds of spectra using R6G as a probe molecule in different concentrations (10^{-18} to 10^{-6} mol L^{-1}), as depicted in Figure 6a,b. The complete set of SERS/SIERS spectra is shown in Figures S11 and S12.

The R6G SERS spectrum in Figure 6a,b is characterized by the prominent bands at 612 cm^{-1} corresponding to the C−C ring in-plane bending in xanthene/phenyl rings, 772 cm^{-1} is attributed to the C−H out-of-plane bending, 1126 cm^{-1} is attributed to the C−H in-plane bending in xanthene/phenyl rings, 1182 cm^{-1} to C−H in-plane bending in xanthene ring, 1312 cm^{-1} to the hybrid mode of xanthene/phenyl rings and NHC$_2$H$_5$ group, and 1597 cm^{-1} to the hybrid mode of phenyl ring with COOC$_2$H$_5$ group. The bands at 1362, 1511, and 1650 cm^{-1} were assigned to the C−C stretching in xanthene rings and 1573 cm^{-1} to the C−C stretching in phenyl ring.[41−43] Figure 6a corresponds to the average SERS spectra for R6G in the range concentration from 10^{-6} to 10^{-18} mol L^{-1} for V-shaped Si microchannel substrates modified with AuNRs. Compared to the flat Si substrate modified with AuNRs in Figure 6b, the lowest R6G detected concentration was 10^{-10} mol L^{-1}, while that of the V-shaped Si substrate with AuNRs enabled attomolar detection (10^{-18} mol L^{-1}). The effective performance of SERS/SIERS substrates can also be evaluated by the AEF, obtained from average intensities for the R6G band position at 1510 cm^{-1}. An AEF of 6.3×10^6 was obtained for flat Si substrate, and 3.3×10^{14} for the V-shaped Si microchannel. We also evaluated the flat Si substrate having high density of AuNRs aggregates, called coffee ring region, with SERS spectra mapping and SEM images illustrated in Figure S13. 10^{-10} mol L^{-1} is the lower concentration detected with reasonable reproducibility in different regions, with obtained AEF value still lower than that obtained for the V-shaped microchannel (AEF = 1.1×10^8). The AEF equation is

included in the Supporting Information. Compared to the literature, V- and W-shaped cavities show AEF values of 2.99×10^5 and 9.97×10^5, respectively.[28] We believe that the excellent result for AEF in this work is directly related to the electric distribution that can vary according to dimension, shape, and dielectric permittivity of the surface.

To better visualize the collection of hundreds spectra, CS, SM, IDMAP, and LSP techniques were used to convert the whole Raman spectrum (1100−1700 cm^{-1}) to a single-colored dot of the visualization map, Figure 6c,d. It was observed that the four techniques were not capable of discriminating the different concentrations of the R6G solution due to the scatter effects, Figure S14 (see the Supporting Information). This problem was solved by applying the EMSC in all spectra. Figure S15a,b depicts the parallel coordinate plot of raw and corrected data, respectively, to demonstrate the efficacy of scattering effect correction. Figure S15c shows that the calculated silhouette coefficient values were negative for all raw data (−0.025, −0.085, −0.096, and −0.096), meaning no discrimination of samples.[44] However, it increased to 0.83 for corrected data, which means that strong discrimination was obtained with the CS technique for the V-shaped Si substrate and 0.77 for the flat Si substrate modified with AuNRs. Figure 6c, the 100 Raman spectra present close-packed clusters for the high concentration of R6G solution, and it starts to disperse with dilution because of spectra noise/resolution. Interestingly, for the V-shaped Si substrate, this phenomenon occurs for concentrations lower than 10^{-16} mol L^{-1}, while for the flat Si substrate, the 10^{-10} mol L^{-1} concentration already presented such dispersion due to the low sensitivity of the system. The system sensitivity can be compared in Figure S16, where the concentrations of 10^{-6} and 10^{-8} mol L^{-1} for the flat Si substrate are equivalent to the responses at concentrations of $\sim10^{-10}$ and 10^{-11} mol L^{-1} for the V-shaped Si substrate. Therefore, the excellent sensitivity and high performance of V-shaped Si substrates are achieved by the combination of SIERS and SERS effects. The synergy between these two effects is crucial to improve the functions of AuNRs in the enhancement of Raman signal and achieve single-molecule detection. The SIERS effect can also improve functionalities of nanoparticles having different morphologies, such as pyramid, cube, nanostar, sphere, and several others. Therefore, more investigation is necessary to expand the comprehension of this effect influencing the electric field distribution created by cavities shaped in the substrate, paving the way for reliable, reproducible SERS substrates.

4. CONCLUSIONS

In conclusion, we demonstrated that the effect based on the SIERS improves the AuNR functions as SERS substrates. Finite-element simulation data for the scattered electric field confirm that the SIERS effects provide constructive interferences patterns explicitly generated by the V-shaped geometric design, occurring in both the cavity and its vicinity. The bare V-shaped Si substrate displayed a Raman signal enhancement of 1.82 times larger than flat Si substrate and 4.29 times with R6G molecules in the absence of AuNRs. The synergy of SIERS and SERS effects in the V-shaped Si substrate modified with AuNRs is the key feature to improve the performance of the SERS substrate, with high reproducibility and sensitivity to achieve attomolar R6G detection. The statistical projection of SERS spectra evidences the high sensitivity with a silhouette coefficient of 0.83 achieved by the V-shaped Si substrate

having AuNRs. The concentrations of 10^{-6} to 10^{-8} mol L^{-1} for the flat Si substrates are approximately equivalent to the responses observed at 10^{-10} to 10^{-11} mol L^{-1} in the V-shaped Si substrates. The calculated AEF value was 6.3×10^6 for the flat Si substrate and 3.3×10^{14} for the V-shaped Si microchannel. Our findings show that the combination of the V-shaped Si microchannel array and AuNRs may provide precisely patterned SERS/SIERS substrates that are promising candidates to evaluate tiny scattering cross-sectional bio-molecule fingerprints toward single-molecule detection.

■ ASSOCIATED CONTENT

Ⓢ Supporting Information

The Supporting Information is available free of charge at https://pubs.acs.org/doi/10.1021/acsami.1c08480.

■ AUTHOR INFORMATION

Corresponding Author

Italo Odone Mazali − *Laboratory of Functional Materials, Institute of Chemistry, University of Campinas—UNICAMP, 13083-970 Campinas, São Paulo, Brazil;* ⓞ orcid.org/0000-0001-5698-5273; Email: mazali@unicamp.br

Authors

Jaciara Bär − *Laboratory of Functional Materials, Institute of Chemistry, University of Campinas—UNICAMP, 13083-970 Campinas, São Paulo, Brazil*

Anerise de Barros − *Laboratory of Functional Materials, Institute of Chemistry, University of Campinas—UNICAMP, 13083-970 Campinas, São Paulo, Brazil;* ⓞ orcid.org/0000-0002-1616-2368

Davi H. S. de Camargo − *Brazilian Nanotechnology National Laboratory (LNNano), Brazilian Center for Research in Energy and Materials (CNPEM), 13083-100 Campinas, São Paulo, Brazil*

Mariane P. Pereira − *Brazilian Nanotechnology National Laboratory (LNNano), Brazilian Center for Research in Energy and Materials (CNPEM), 13083-100 Campinas, São Paulo, Brazil*

Leandro Merces − *Brazilian Nanotechnology National Laboratory (LNNano), Brazilian Center for Research in Energy and Materials (CNPEM), 13083-100 Campinas, São Paulo, Brazil;* ⓞ orcid.org/0000-0002-6202-9824

Flavio Makoto Shimizu − *Brazilian Nanotechnology National Laboratory (LNNano), Brazilian Center for Research in Energy and Materials (CNPEM), 13083-100 Campinas, São Paulo, Brazil; Department of Applied Physics, "Gleb Wataghin" Institute of Physics (IFGW), University of Campinas (UNICAMP), 13083-859 Campinas, São Paulo, Brazil;* ⓞ orcid.org/0000-0002-4833-9893

Fernando A. Sigoli − *Laboratory of Functional Materials, Institute of Chemistry, University of Campinas—UNICAMP, 13083-970 Campinas, São Paulo, Brazil;* ⓞ orcid.org/0000-0003-1285-6765

Carlos César Bof Bufon − *Brazilian Nanotechnology National Laboratory (LNNano), Brazilian Center for Research in Energy and Materials (CNPEM), 13083-100*

Campinas, São Paulo, Brazil; ● orcid.org/0000-0002-1493-8118

■ REFERENCES

(1) Alvarez-Puebla, R. A.; Liz-Marzán, L. M. SERS-Based Diagnosis and Biodetection. *Small* **2010**, *6*, 604–610.

(2) Alves, R. S.; Sigoli, F. A.; Mazali, I. O. Aptasensor Based on a Flower-Shaped Silver Magnetic Nanocomposite Enables the Sensitive and Label-Free Detection of Troponin I (CTnI) by SERS. *Nanotechnology* **2020**, *31*, 505505.

(3) Godoy, N. V.; García-Lojo, D.; Sigoli, F. A.; Pérez-Juste, J.; Pastoriza-Santos, I.; Mazali, I. O. Ultrasensitive Inkjet-Printed Based SERS Sensor Combining a High-Performance Gold Nanosphere Ink and Hydrophobic Paper. *Sens. Actuators, B* **2020**, *320*, 128412.

(4) Lane, L. A.; Qian, X.; Nie, S. SERS Nanoparticles in Medicine: From Label-Free Detection to Spectroscopic Tagging. *Chem. Rev.* **2015**, *115*, 10489–10529.

(5) Pastorello, M.; Sigoli, F. A.; dos Santos, D. P.; Mazali, I. O. On the Use of Au@Ag Core-Shell Nanorods for SERS Detection of Thiram Diluted Solutions. *Spectrochim. Acta, Part A* **2020**, *231*, 118113.

(6) Sun, Y.; Zhai, X.; Xu, Y.; Liu, C.; Zou, X.; Li, Z.; Shi, J.; Huang, X. Facile Fabrication of Three-Dimensional Gold Nanodendrites Decorated by Silver Nanoparticles as Hybrid SERS-Active Substrate for the Detection of Food Contaminants. *Food Control* **2021**, *122*, 107772.

(7) Wang, Y.; Yan, B.; Chen, L. SERS Tags: Novel Optical Nanoprobes for Bioanalysis. *Chem. Rev.* **2013**, *113*, 1391–1428.

(8) Yang, S.; Dai, X.; Stogin, B. B.; Wong, T.-S. Ultrasensitive Surface-Enhanced Raman Scattering Detection in Common Fluids. *Proc. Natl. Acad. Sci. U.S.A.* **2016**, *113*, 268–273.

(9) Zong, C.; Xu, M.; Xu, L.-J.; Wei, T.; Ma, X.; Zheng, X.-S.; Hu, R.; Ren, B. Surface-Enhanced Raman Spectroscopy for Bioanalysis: Reliability and Challenges. *Chem. Rev.* **2018**, *118*, 4946–4980.

(10) Jeanmaire, D. L.; Van Duyne, R. P. Surface Raman Spectroelectrochemistry: Part I Heterocyclic, Aromatic, and Aliphatic Amines Adsorbed on the Anodized Silver Electrode. *J. Electroanal. Chem.* **1977**, *84*, 1.

(11) Albrecht, M. G.; Creighton, J. A. Anomalously Intense Raman Spectra of Pyridine at a Silver Electrode. *J. Am. Chem. Soc.* **1977**, *99*, 5215–5217.

(12) Fleischmann, M.; Hendra, P. J.; McQuillan, A. J. Raman Spectra of Pyridine Adsorbed at a Silver Electrode. *Chem. Phys. Lett.* **1974**, *26*, 163–166.

(13) Le Ru, E. C.; Etchegoin, P. G. Quantifying SERS Enhancements. *MRS Bull.* **2013**, *38*, 631–640.

(14) Shvalya, V.; Filipič, G.; Zavašnik, J.; Abdulhalim, I.; Cvelbar, U. Surface-Enhanced Raman Spectroscopy for Chemical and Biological Sensing Using Nanoplasmonics: The Relevance of Interparticle Spacing and Surface Morphology. *Appl. Phys. Rev.* **2020**, *7*, 031307.

(15) Srivastava, S. K.; Li, A.; Li, S.; Abdulhalim, I. Optimal Interparticle Gap for Ultrahigh Field Enhancement by LSP Excitation via ESPs and Confirmation Using SERS. *J. Phys. Chem. C* **2016**, *120*, 28735–28742.

(16) Zhang, D.; You, H.; Zhang, L.; Fang, J. Facile Surface Modification of Mesoporous Au Nanoparticles for Highly Sensitive SERS Detection. *Anal. Chem.* **2020**, *92*, 15379–15387.

(17) Koetz, J. The Effect of Surface Modification of Gold Nanotriangles for Surface-Enhanced Raman Scattering Performance. *Nanomaterials* **2020**, *10*, 2187.

(18) Hanske, C.; Hill, E. H.; Vila-Liarte, D.; González-Rubio, G.; Matricardi, C.; Mihi, A.; Liz-Marzán, L. M. Solvent-Assisted Self-Assembly of Gold Nanorods into Hierarchically Organized Plasmonic Mesostructures. *ACS Appl. Mater. Interfaces* **2019**, *11*, 11763–11771.

(19) Jones, S. T.; Taylor, R. W.; Esteban, R.; Abo-Hamed, E. K.; Bomans, P. H. H.; Sommerdijk, N. A. J. M.; Aizpurua, J.; Baumberg, J. J.; Scherman, O. A. Gold Nanorods with Sub-Nanometer Separation Using Cucurbit[n]Uril for SERS Applications. *Small* **2014**, *10*, 4298–4303.

(20) de Barros, A.; Shimizu, F. M.; de Oliveira, C. S.; Sigoli, F. A.; dos Santos, D. P.; Mazali, I. O. Dynamic Behavior of Surface-Enhanced Raman Spectra for Rhodamine 6G Interacting with Gold Nanorods: Implication for Analyses under Wet versus Dry Conditions. *ACS Appl. Nano Mater.* **2020**, *3*, 8138–8147.

(21) Liu, H.; Yang, Z.; Meng, L.; Sun, Y.; Wang, J.; Yang, L.; Liu, J.; Tian, Z. Three-Dimensional and Time-Ordered Surface-Enhanced Raman Scattering Hotspot Matrix. *J. Am. Chem. Soc.* **2014**, *136*, 5332–5341.

(22) Zhou, Q.; Kim, T. Review of Microfluidic Approaches for Surface-Enhanced Raman Scattering. *Sens. Actuators, B* **2016**, *227*, 504–514.

(23) Michon, J.; Kita, D.; Hu, J. Sensitivity Comparison of Free-Space and Waveguide Raman for Bulk Sensing. *J. Opt. Soc. Am. B* **2020**, *37*, 2012–2020.

(24) Gu, Y.; Xu, S.; Li, H.; Wang, S.; Cong, M.; Lombardi, J. R.; Xu, W. Waveguide-Enhanced Surface Plasmons for Ultrasensitive SERS Detection. *J. Phys. Chem. Lett.* **2013**, *4*, 3153–3157.

(25) Li, S.; Xia, L.; Yang, Z.; Zhou, M.; Zhao, B.; Li, W. Hybrid Plasmonic Grating Slot Waveguide with High Field Enhancement for an On-Chip Surface-Enhanced Raman Scattering Sensor. *Appl. Opt.* **2020**, *59*, 748–755.

(26) Li, Y.; Zhao, H.; Raza, A.; Clemmen, S.; Baets, R. Surface-Enhanced Raman Spectroscopy Based on Plasmonic Slot Waveguides With Free-Space Oblique Illumination. *IEEE J. Quantum Eletronics* **2020**, *56*, 1–8.

(27) Ding, S.-Y.; You, E.-M.; Tian, Z.-Q.; Moskovits, M. Electromagnetic Theories of Surface-Enhanced Raman Spectroscopy. *Chem. Soc. Rev.* **2017**, *46*, 4042–4076.

(28) Li, N.; Feng, L.; Teng, F.; Lu, N. Fabrication of Plasmonic Cavity Arrays for SERS Analysis. *Nanotechnology* **2017**, *28*, 185301.

(29) Wu, S.; Shen, Y.; Jin, C. Surface-Enhanced Raman Scattering Induced by the Coupling of the Guided Mode with Localized Surface Plasmon Resonances. *Nanoscale* **2019**, *11*, 14164–14173.

(30) Maimaiti, A.; Patra, P. P.; Jones, S.; Antosiewicz, T. J.; Verre, R. Low-Loss Hybrid High-Index Dielectric Particles on a Mirror for Extreme Light Confinement. *Adv. Opt. Mater.* **2020**, *8*, 1901820.

(31) Murphy, D. V.; Brueck, S. R. J. Enhanced Raman Scattering from Silicon Microstructures. *Opt. Lett.* **1983**, *8*, 494–496.

(32) Zaidi, S. H.; Chu, A. S.; Brueck, S. R. J. Optical Properties of Nanoscale, One- Dimensional Silicon Grating Structures. *J. Appl. Phys.* **1996**, *80*, 6997–7008.

(33) Mamichev, D. A.; Timoshenko, V. Y.; Zoteyev, A. V.; Golovan, L. A.; Krutkova, E. Y.; Laktyunkin, A. V.; Kashkarov, P. K.; Astrova, E. V.; Perova, T. S. Enhanced Raman Scattering in Grooved Silicon Matrix. *Phys. Status Solidi B* **2009**, *246*, 173–176.

(34) Ashkar, R.; Hore, M. J. A.; Ye, X.; Natarajan, B.; Greybush, N. J.; Lam, T.; Kagan, C. R.; Murray, C. B. Rapid Large-Scale Assembly and Pattern Transfer of One-Dimensional Gold Nanorod Super-structures. *ACS Appl. Mater. Interfaces* **2017**, *9*, 25513−25521.

(35) Torgerson, W. S. Multidimensional Scaling of Similarity. *Psychometrika* **1965**, *30*, 379−393.

(36) Minghim, R.; Paulovich, F. V.; de Andrade Lopes, A. Content-Based Text Mapping Using Multi-Dimensional Projections for Exploration of Document Collections. *Visualization and Data Analysis 2006*, 2006; Vol. *6060*, pp 1−12.

(37) Sammon, J. W. A Nonlinear Mapping for Data Structure Analysis. *IEEE Trans. Comput.* **1969**, *18*, 401−409.

(38) Paulovich, F. V.; Nonato, L. G.; Minghim, R.; Levkowitz, H. Least Square Projection: A Fast High-Precision Multidimensional Projection Technique and Its Application to Document Mapping. *IEEE Trans. Vis. Comput. Graph.* **2008**, *14*, 564−575.

(39) Paulovich, F. V.; Moraes, M. L.; Maki, R. M.; Ferreira, M.; Oliveira, O. N.; de Oliveira, M. C. F. Information Visualization Techniques for Sensing and Biosensing. *Analyst* **2011**, *136*, 1344−1350.

(40) Lu, J.; Song, Y.; Lei, F.; Du, X.; Huo, Y.; Xu, S.; Li, C.; Ning, T.; Yu, J.; Zhang, C. Electric Field-Modulated Surface Enhanced Raman Spectroscopy by PVDF/Ag Hybrid. *Sci. Rep.* **2020**, *10*, 5269.

(41) Watanabe, H.; Hayazawa, N.; Inouye, Y.; Kawata, S. DFT Vibrational Calculations of Rhodamine 6G Adsorbed on Silver: Analysis of Tip-Enhanced Raman Spectroscopy. *J. Phys. Chem. B* **2005**, *109*, 5012−5020.

(42) Virga, A.; Rivolo, P.; Frascella, F.; Angelini, A.; Descrovi, E.; Geobaldo, F.; Giorgis, F. Silver Nanoparticles on Porous Silicon: Approaching Single Molecule Detection in Resonant SERS Regime. *J. Phys. Chem. C* **2013**, *117*, 20139−20145.

(43) Zhong, F.; Wu, Z.; Guo, J.; Jia, D. Porous Silicon Photonic Crystals Coated with Ag Nanoparticles as Efficient Substrates for Detecting Trace Explosives Using SERS. *Nanomaterials* **2018**, *8*, 872.

(44) Rousseeuw, P. J. Silhouettes: A Graphical Aid to the Interpretation and Validation of Cluster Analysis. *J. Comput. Appl. Math.* **1987**, *20*, 53−65.